Electronic Supplementary Material (ESI) for Energy & Environmental Science.

Supplementary Information

for

Weakened *d-p* Orbital Hybridization in *In Situ* Reconstructed Ru/β-$Co(OH)_2$ Heterointerfaces for Accelerated Ammonia Electrosynthesis from Nitrates

Weijie Zhu,[a†] Fen Yao,[b†] Qiongfei Wu,[a] Qiu Jiang,[c] Jinxian Wang,[d] Zhoucheng Wang,[a] Hanfeng Liang[a, e*]

[a]State Key Laboratory of Physical Chemistry of Solid Surfaces, College of Chemistry and Chemical Engineering, Xiamen University, Xiamen 361005, China

[b]Key Laboratory of Preparation and Applications of Environmentally Friendly Material of the Ministry of Education, College of Chemistry, Jilin Normal University, Changchun 130103, China

[c]School of Materials and Energy, University of Electronic Science and Technology of China, Chengdu 611731, China

[d]School of Chemistry and Environmental Engineering, Changchun University of Science and Technology, Changchun 130022, China

[e]Innovation Laboratory for Sciences and Technologies of Energy Materials of Fujian Province (IKKEM), Xiamen 361005, China

†These authors contributed equally to this work.

*Corresponding author. Email: hfliang@xmu.edu.cn

Experimental section

Material and chemicals. Cobalt nitrate hexahydrate [$Co(NO_3)_2·6H_2O$], potassium hydroxide (KOH, ≥85% content), potassium nitrate (KNO_3), magnesium chloride hexahydrate ($MgCl_2·6H_2O$) and phosphoric acid (H_3PO_4) were purchased from Sinopharm Chemical Reagent Co., Ltd. Ammonia, nitrate and nitrite standard solutions as well as hydroquinone and deuterated dimethylsulfoxide (DMSO-d6) were purchased from Shanghai Aladdin Biochemical Technology Co., Ltd. Ruthenium chloride hydrate ($RuCl_3·xH_2O$, 37% Ru basis) and commercial 5 wt% Ru/C were purchased from Shanghai Maclin Biochemical Technology Co., Ltd. Carbon papers (CPs, TGP-H-060, 0.19 mm thickness), Zn foils (0.2 mm thickness) and Dupont proton exchange membranes (Nafion N212, N117) were purchased from Suzhou Sinero Technology Co. Ltd. Electrochemical equipment was purchased from Shanghai Yueci Electronic Technology Co., Ltd. Membrane electrode assembly was purchased from Changsha Spring New Energy Technology Co., Ltd. The distilled water (10-15 MΩ·cm) used throughout all experiments was purified through a Millipore system.

Preparation of Ru-doped Co metal (named as RuCo thereafter) nanosheets on CP. The preparation of RuCo nanosheets on CP was based on a combined method of cation exchange and thermal reduction. $Co(OH)_2$ nanosheets were first electrodeposited onto a carbon paper using a standard three-electrode configuration, wherein a 1×1.5 cm^2 CP, a 1×1.5 cm^2 Pt sheet and a saturated calomel electrode (SCE) were employed as working, counter and reference electrodes, respectively. The electrolyte was 200 mL of 0.05 M $Co(NO_3)_2$ aqueous solution. The electrodeposition procedure was controlled at -1 V *vs.* SCE for 10 min to form the $Co(OH)_2$ nanosheets, which was then rinsed with distilled water and dried in the oven at 60 °C. Afterwards, the $Co(OH)_2$ nanosheets on CP was calcined in the muffle electric furnace at 300 °C for 3 h with a heating rate of 5 °C min^{-1} to form Co_3O_4 nanosheets. After that, four pieces of Co_3O_4 nanosheets on CPs were vertically immersed in 60 mL of 0.1 mg mL^{-1} $RuCl_3$ aqueous solution at 60 °C with a stirring rate of 300 rpm to initiate a cation exchange reaction ($Co_3O_4 + Ru^{3+} + yH_2O \rightarrow RuCoO_x·yH_2O + Co^{3+}$) driven by the slow acidic etching (the pH of 0.1 mg mL^{-1} $RuCl_3$ aqueous solution was *ca.* 2.20). Until the suspended Ru species particles were observed in the solution, the obtained precursors were then rinsed, dried, and eventually calcined in a tube furnace at 300 °C for 3 h with a heating rate of 5 °C min^{-1} under the 10% H_2/Ar mixed gas to form the RuCo nanosheets. The typical mass loading of Ru and Co, determined by inductively coupled plasma mass spectrometry (ICP-MS), were *ca.* 0.0809 and 1.5324 mg cm^{-2}, respectively.

Preparation of Co metal nanosheets on CP. The as-prepared $Co(OH)_2$ nanosheets on CP was directly calcined in a tube furnace at 300 °C for 3 h with a heating rate of 5 °C min^{-1} under the 10% H_2/Ar mixed gas to form the Co metal nanosheets on CP. The mass loading of Co was *ca.* 1.6208 mg cm^{-2}, determined by ICP-MS.

Preparation of Ru metal nanoparticles on CP. The Ru metal nanoparticles were directly electrodeposited on CP. Specifically, the electrodeposition process was conducted at -10 mA cm^{-2} for 15 min in an electrolytic cell, where 60 mL of 1 mg mL^{-1} $RuCl_3$ aqueous solution, a 1×1.5 cm^2 CP and a 1×1.5 cm^2 Pt sheet were employed as electrolyte, working, and counter electrodes, respectively. In order to exclude the effect of crystallinity, the obtained Ru metal nanoparticles was further calcined in a tube furnace at 300 °C for 3 h with a heating rate of 5 °C min^{-1} under the 10% H_2/Ar mixed gas to improve the crystallinity. The mass loading of Ru was *ca.* 0.1426 mg cm^{-2}, determined by ICP-MS.

Preparation of heterogeneous interfacial Ru@Co(OH)$_2$ composite on CP. The synthetic method of Ru@Co(OH)$_2$ was same as that of Ru metal nanoparticles on CP except that the CP substrate had been covered by the electrodeposited Co(OH)$_2$ nanosheets and the subsequent calcination process was absent.

Preparation of Ru/C on CP. 1.5 mg commercial 5 wt% Ru/C powder was ultrasonically dispersed in a mixed solution containing 100 μL distilled water, 100 μL isopropanol, and 10 μL 5 wt% Nafion solution with an ultrasonic powder of 40 kHz for at least 1 h to form the homogeneous ink. Then the whole ink was drop-casted onto a piece of CP (1×1 cm^2) under the infrared heating lamp.

Preparation of two-phase Ru/C-Co(OH)$_2$ mixture on CP. The preparation method of two-phase Ru/C-Co(OH)$_2$ mixture was the same as that of Ru/C on CP except that the CP substrate had been covered by the electrodeposited Co(OH)$_2$ nanosheets.

Physical characterizations. Scanning electron microscopy (SEM) images were collected by a ZEISS Sigma microscope. Transmission electron microscopy (TEM), high-angle annular dark-field scanning TEM (HAADF-STEM) images and energy dispersive spectrometer (EDS) spectra were obtained on a FEI Tecnai F30. X-ray diffraction (XRD) patterns were recorded by a Rigaku Ultima-IV XRD with Cu-Kα radiation (λ = 1.5405 Å). X-ray photoelectron spectroscopy (XPS) spectra were collected on a Thermo Fisher Escalab Xi+ with Al-Kα as radiation source. Nitrogen adsorption-desorption isotherms and pore distribution plots were obtained by an automatic physical adsorption apparatus (ASAP2460). ICP-MS were conducted on an Agilent 7800. Ammonia, nitrate and nitrite concentrations were determined by a 850 professional ion chromatography (IC). ^{15}N isotopically labeled ammonia concentration was also detected by ^{1}H nuclear magnetic resonance (NMR) spectroscopy on a Bruker Avance III 500 MHz. *In situ* Raman test was conducted on a Renishaw inVia confocal Raman microscope under an excitation of 532 nm laser with the power of 4.0 mW.

Electrochemical tests. Nitrate reduction reaction (NtrRR) tests were conducted by CHI

660E electrochemical workstation (Chenhua, Shanghai) in a standard H-type electrolytic cell, in which a self-supported catalyst on CP, a Pt sheet, a pristine HgO/Hg electrode and a N117 proton exchange membrane were employed as working, counter, reference electrodes and diaphragm, respectively. Anolyte and catholyte were 50 mL of 1 M KOH and 1 M KOH/0.1 M KNO_3 mixed electrolyte, respectively, unless otherwise specified. They were kept stirring throughout the tests to minimize the mass transfer limitation. Initially successive linear sweep voltammetry (LSV) of each electrode was conducted at a rate of 5 mV s^{-1} to stabilize the electrodes (till the LSV curves do not show significant variation), and the last curve was used to compare activity of the electrocatalysts. A typical example can be seen in Fig. S9, ESI†. All the potentials were converted into reversible hydrogen potential (RHE) by Nernst equation with iR_s compensation by the following formula.

$$E_{vs.\mathrm{RHE}} = E_{vs.\mathrm{HgO/Hg}} + 0.0592 \times \mathrm{pH} + 0.098\ \mathrm{V} - iR_s \tag{S1}$$

where R_s is the solution impedance, obtained by the impedance tests.

Chronoamperometry and chronopotentiometry were conducted to evaluate the NtrRR Faradaic efficiency. The electrolytes after tests were injected into IC to measure the ammonia, nitrate and nitrite concentrations. The Faradaic efficiency of ammonia or nitrite production and the ammonia production rate were calculated as follows.

Faraday efficiency: $$FE = \frac{nzF}{it} \times 100\% \tag{S2}$$

Ammonia production rate: $$Q = \frac{n}{tA} \tag{S3}$$

where n, z, F, i, t and A are moles of products (mol), transferred electron number (2 for nitrite or 8 for ammonia), Faraday constant (96485 C mol^{-1}), current (A), time (s) and geometric area of electrodes (cm^2), respectively.

It is noted that the electrode area was reduced to 0.5 cm × 0.5 cm during the long-term stability test under -250 mA cm^{-2} because of the rapid depletion of nitrate under high currents while the electrode area was reduced to 1 cm × 0.5 cm during the chronopotentiometry test under -500 mA cm^{-2} due to the current limitation of CHI 660E electrochemical workstation.

The nitrate purification experiments were conducted at 0 V *vs.* RHE (without iR_s correction) in 1 M KOH electrolytes with different nitrate concentrations.

Hydrogen evolution reaction (HER) tests were also conducted in the same H-type electrolytic cell except that the catholyte was replaced by 50 mL of 1 M KOH. Polarization curves were collected in the same way.

Assembly of Zn-nitrate flow battery. The Zn-nitrate flow battery was assembled in a membrane electrode assembly flow reactor, wherein two pieces of stacked self-supported RuCo catalysts on CPs (1 cm × 1 cm), ten pieces of commercial Zn foils (0.8 cm × 1.5 cm) and a proton exchange membrane (Nafion N212) were directly used as cathode, anode and diaphragm, respectively. It is noted that the stacked Zn foils can prolong the lifespan of the Zn-nitrate flow battery. The bipolar plates were high-purity titanium plates and areas of serpentine flow channels were 1 cm × 2 cm. Catholyte was 100 mL of 1 M KOH/0.1 M KNO_3 mixed electrolyte while anolyte was 100 mL of 6 M KOH and their flow rates were 150 mL min^{-1}. The simulated device diagram can be seen in Fig. 5a. The polarization curves were recorded by chronopotentiometry with or without *iR* calibration. Chronopotentiometry was also used to evaluate the stability of the Zn-nitrate battery, accompanied with ammonia detection.

The discharging power densities were calculated as follows.

$$P = j \times E \tag{S4}$$

where j is current density and E is cell voltage.

Purification of ammonia into struvite product. In this work, we used coprecipitation method to convert the generated ammonia in the electrolyte into high-purity struvite precipitation. Specifically, the pH of the catholyte after the reaction was first adjusted to 9 by 1 M HCl. The equivalent molar amount of $MgCl_2 \cdot 6H_2O$ and H_3PO_4 was then added to the catholyte, after which the pH was stable at 1.3. Afterwards, the pH of the catholyte went back to 9 by adding 1 M KOH. After the solution aged for 1 h, the obtained struvite product was eventually centrifuged, washed and dried.

Determination of ammonia, nitrate and nitrite using IC. In this work, the concentrations of the ammonia, nitrate and nitrite in the electrolyte were quantified by IC, unless otherwise specified. The electrolyte solution was diluted and then directly injected into the IC to measure their concentrations. The standard curves were plotted by diluted standard solution against the peak area of ionic conductivity (Fig. S14, ESI†). The chromatographic filtrate was 5 vol% HNO_3 for cation detection or 1 mM $NaHCO_3$ and 3 mM Na_2CO_3 mixed solution for anion detection. The solution for suppressor was 1 vol% H_3PO_4.

Determination of ammonia using ^{1}H NMR spectroscopy. In order to confirm the origin of ammonia, we also used a ^{15}N isotope-labelling electrolyte. The concentration of the produced ammonia in the ^{15}N or ^{14}N-labeled KNO_3 electrolyte was quantified by ^{1}H NMR spectroscopy. The electrolyte solution was first acidified using 1 M H_2SO_4. Afterwards, the electrolyte (30 μL), mixed with hydroquinone (7.5 mM, 10 μL, internal standard solution) and DMSO-d6 (400 μL), was sealed into an NMR tube for ^{1}H NMR detection. The concentration of NH_4^+ was determined by comparing the integral area of the singlet for hydroquinone with the triplet for $^{14}NH_4^+$ or doublet for $^{15}NH_4^+$.

Theoretical calculations. All the density functional theory (DFT) calculations were conducted with the Vienna Ab-initio Simulation Package (VASP) with the generalized gradient approximation (GGA) of the Perdew-Burke-Ernzerhof (PBE) approach (*Phys. Rev. Lett.* **1996**, *77*, 3865; *Phys. Rev. Lett.* **2008**, *100*, 136406). 500 eV kinetic energy cutoff and 0.05 eV Å^{-1} Hellmann-force threshold were used for accurate optimization of the structural relaxations, respectively. 0.2 eV smearing based on the method of Methfessel-Paxton was used for the total energy calculations. The Brillouin zone integration was performed with 3×1×1 Monkhorst-Pack *k*-point sampling for geometry relaxation. The atomic coordinates of the computational models are displayed in Fig. S27, ESI†. A Ru/β-$Co(OH)_2$ heterostructure was used, which contains 27 Co atoms, 54 O atoms, 54 H atoms and 32 Ru atoms with a 20 Å vacuum gap along the z-direction. The heterostructure was comprised of a *p*(3×3) unit cell of $Co(OH)_2$ (011) surface with 1.5 layers and a *p*(2×2) unit cell of Ru (100) surface with 2 layers. Bader charge analysis was performed to describe the charge variation quantitatively (*J. Phys. Condens. Matter.* **2009**, *21*, 084204). Known as a pre- and postprocessing program for the VASP code, VASPKIT was adopted to obtain the DOS diagrams (*Comput. Phys. Commun.* **2021**, *267*, 108033).

According to the computational hydrogen electrode (CHE) model (*J. Phys. Chem. B*, **2004**, *108*, 17886), the Gibbs free energy change (ΔG) for each elemental step was calculated by

$$\Delta G = \Delta E + \Delta \mathrm{ZPE} - \mathrm{T}\Delta S \qquad \text{(S5)}$$

where ΔE denotes the energy obtained from DFT calculations. ΔZPE and ΔS are the correction of zero-point energy and entropy, respectively. T represents room temperature (298.15 K).

To avoid calculating the energy of charged NO_3^- directly, gaseous HNO_3 is chosen as a reference instead (*ACS Catal.* **2019**, *9*, 7052). The adsorption energy of NO_3^- (ΔG_{*NO3}) is described as

$$\Delta G_{*\mathrm{NO3}} = G_{*\mathrm{NO3}} - G_{*} - [G_{\mathrm{HNO3(g)}} - 1/2G_{\mathrm{H2(g)}}] + \Delta G_{\mathrm{correct}} \qquad \text{(S6)}$$

where $G_{*\mathrm{NO3}}$, G_{*}, $G_{\mathrm{HNO3(g)}}$, and $G_{\mathrm{H2(g)}}$ are the Gibbs free energy of NO_3^- adsorbed on the substrates, HNO_3, and H_2 molecules in the gas phase, respectively. The free energy correction, $\Delta G_{\mathrm{correct}}$, is set to 0.392 eV.

Principle of the reconstruction of the RuCo catalyst. The self-reconstruction of the Co metal to $Co(OH)_2$ in the RuCo catalyst can be attributed to the spontaneous redox reaction between Co and nitrate in base ($3Co + 2NO_3^- + 4H_2O \rightarrow 3Co(OH)_2 + 2NO\uparrow + 2OH^-$). The corresponding driving voltage is *ca.* 0.60 V, and the Gibbs free energy is *ca.* -173.67 kJ mol^{-1}. To verify this principle, we detected the open circuit potential of the RuCo catalyst in 1 M KOH/0.1M KNO_3 and then conducted the XRD test. The open circuit potential curve indicates that the RuCo catalyst undergoes a rapid self-reconstruction process in 1 M KOH/0.1 M KNO_3 with the potential ranging from 0.25 to 0.95 V *vs.* RHE (Fig. S25a, ESI†), almost identical with the Co oxidation peak of the first LSV curve (Fig. S9, ESI†). The post XRD pattern indicates that the Co metal has been transformed into $Co(OH)_2$ (Fig. S25b, ESI†), suggesting the fast reconstruction process. It is noted that the alkaline nitrate solution cannot oxidize Ru metal ($Ru + NO_3^- + 2H_2O \rightarrow Ru(OH)_4^- + NO\uparrow$) due to a negative theoretical driving voltage of *ca.* -0.15 V or a positive Gibbs free energy of *ca.* 43.42 kJ mol^{-1}.

Additional Figures

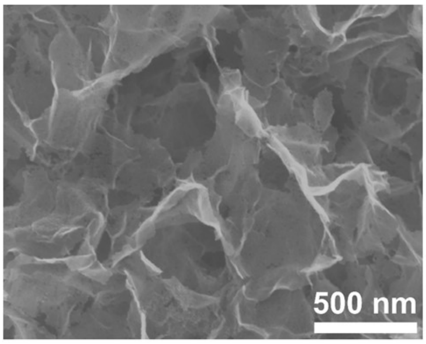

Fig. S1 High-resolution SEM image of the RuCo nanosheets on carbon paper.

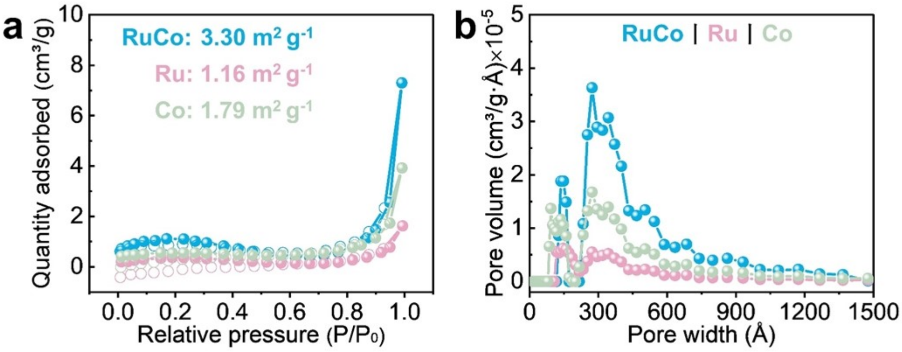

Fig. S2 (a) N_2 adsorption-desorption isotherms and (b) pore distribution plots of the Ru, Co, and RuCo metals on carbon paper.

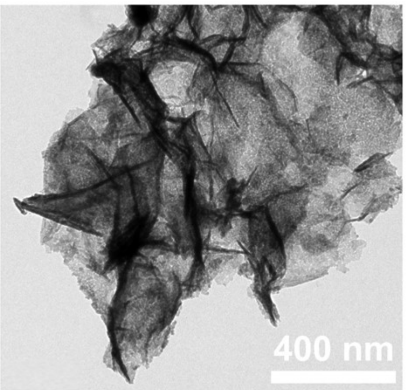

Fig. S3 TEM image of the RuCo nanosheets.

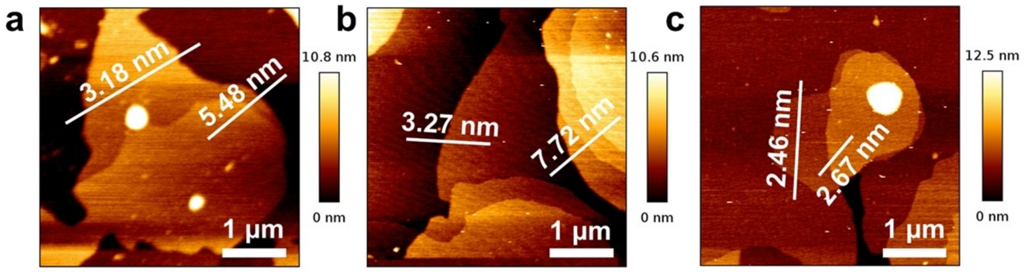

Fig. S4 AFM images of the RuCo nanosheets.

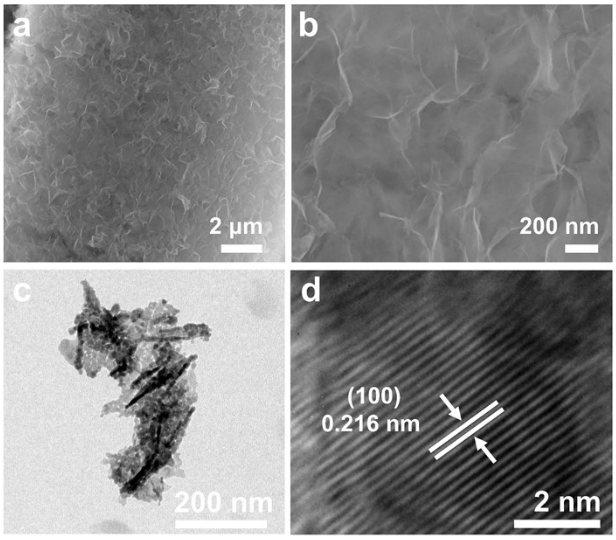

Fig. S5 (a, b) SEM, (c) TEM, and (d) HRTEM images of the Co nanosheets on carbon paper.

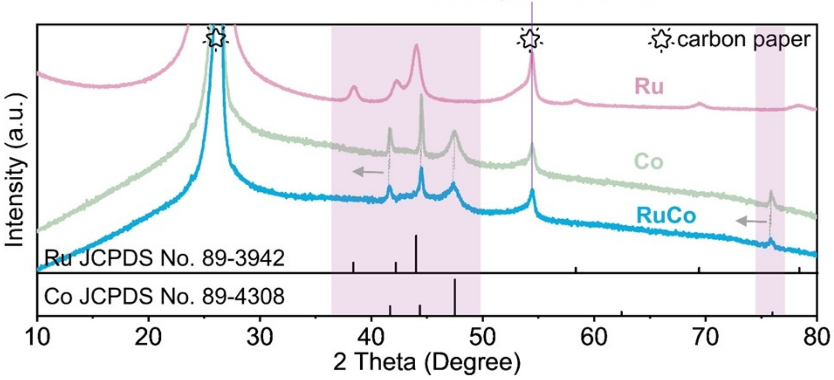

Fig. S6 XRD patterns of the Ru, Co, and RuCo metals on carbon paper.

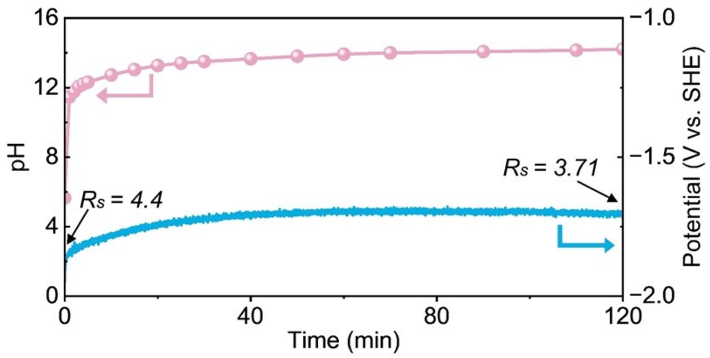

Fig. S7 Chronopotentiometry (without RHE conversion and iR_s correction) and pH curves of the RuCo catalyst in a single chamber electrolytic cell in 0.5 M KNO_3 electrolyte under -250 mA cm^{-2}.

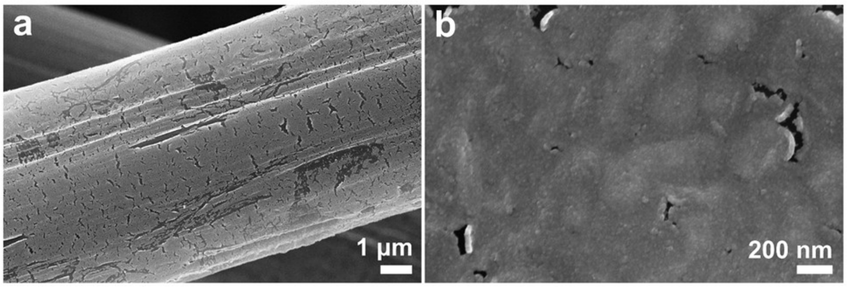

Fig. S8 SEM images of the Ru metal on carbon paper.

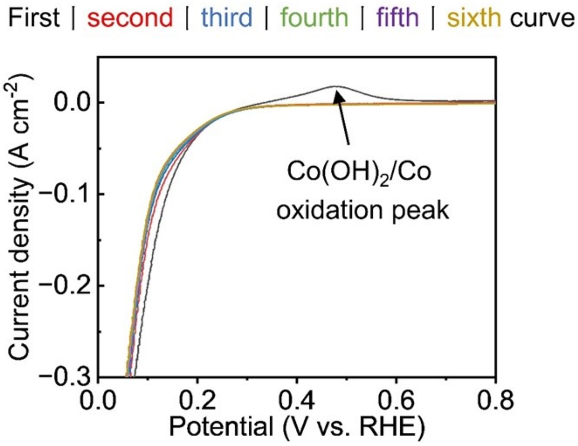

Fig. S9 Continuous LSV curves of the RuCo catalyst in a 1 M KOH/0.1 M KNO_3 electrolyte.

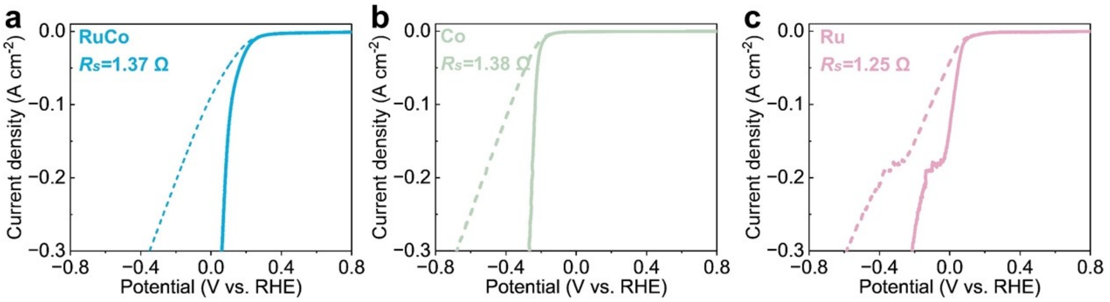

Fig. S10 LSV curves of (a) RuCo, (b) Co and (c) Ru metals with (solid line) or without (dotted line) iR_s correction in a 1 M KOH/0.1 M KNO_3 electrolyte.

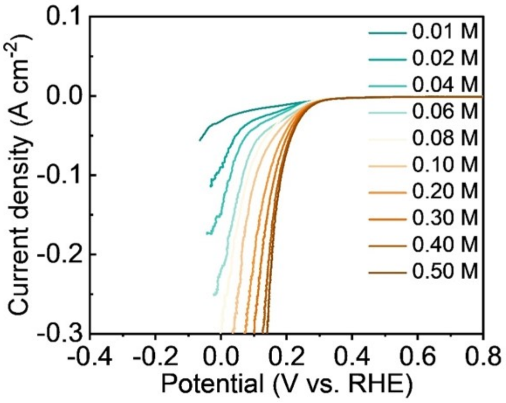

Fig. S11 LSV curves of the RuCo catalyst in 1 M KOH mixed with different nitrate concentrations.

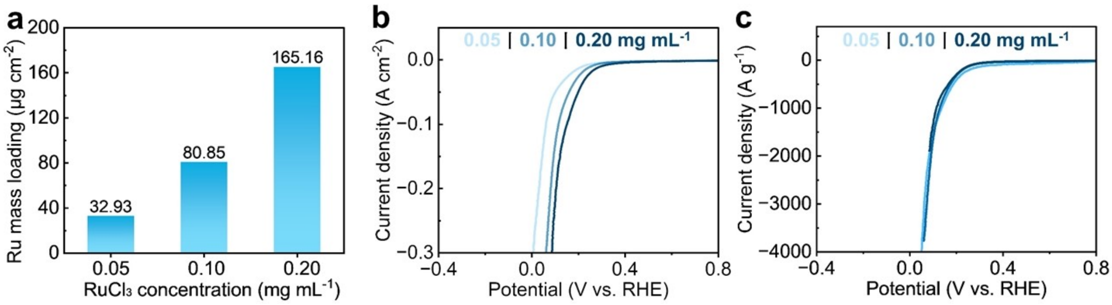

Fig. S12 (a) Ru mass loading of the RuCo catalyst by adjusting $RuCl_3$ concentrations during the synthesis process. LSV curves normalized by (b) geometric area and (c) mass of the RuCo catalyst with different mass loading in a 1 M KOH/0.1 M KNO_3

electrolyte.

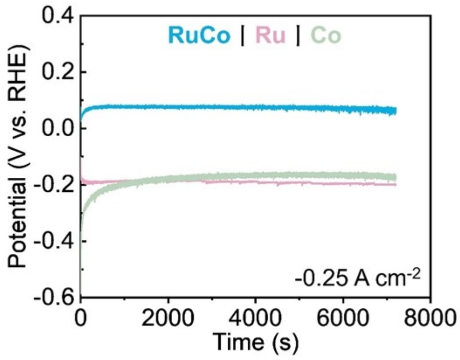

Fig. S13 Chronopotentiometry curves of the RuCo, Ru and Co metals under -250 mA cm^{-2} in a 1 M KOH/0.1 M KNO_3 mixed electrolyte.

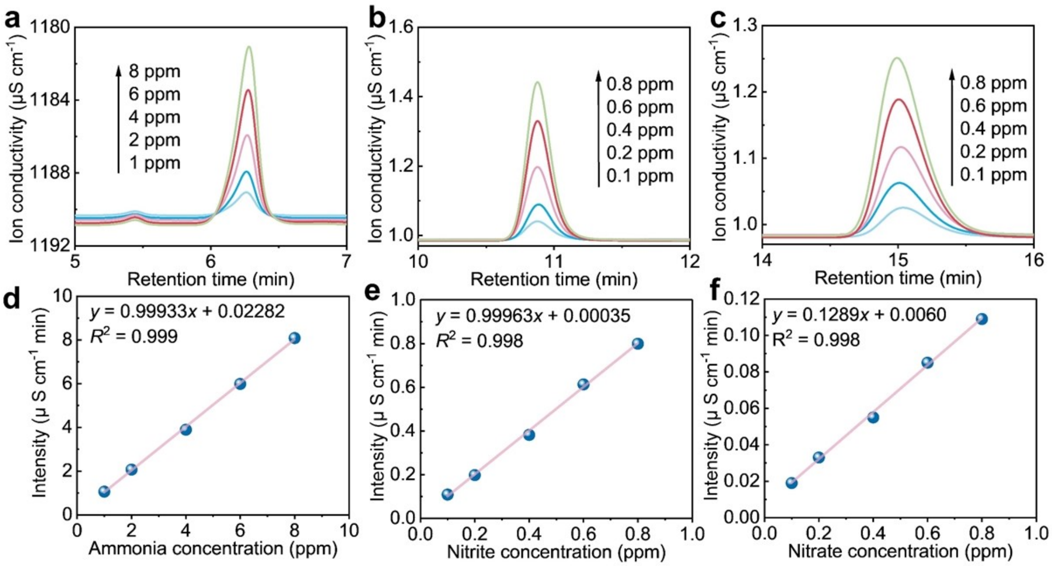

Fig. S14 (a, b, c) IC signal curves and (d, e, f) the plotted standard curves of ammonia, nitrite and nitrate.

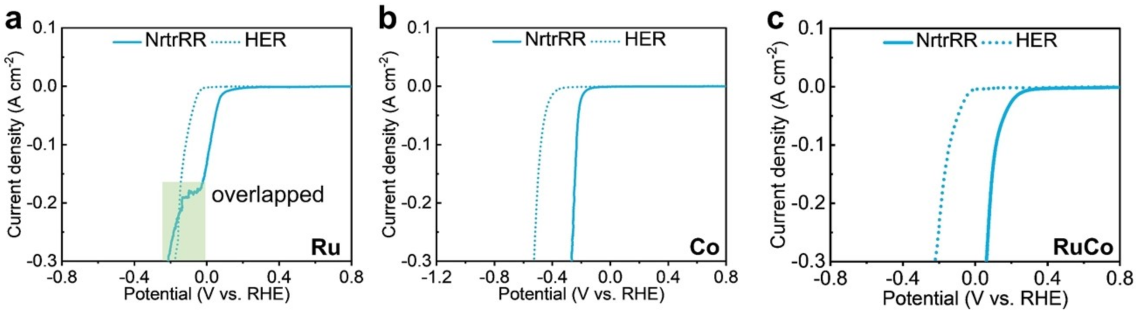

Fig. S15 HER and NtrRR polarization curves of (a) the Ru, (b) Co and (c) the RuCo metals in a 1 M KOH electrolyte with or without 0.1 M KNO_3.

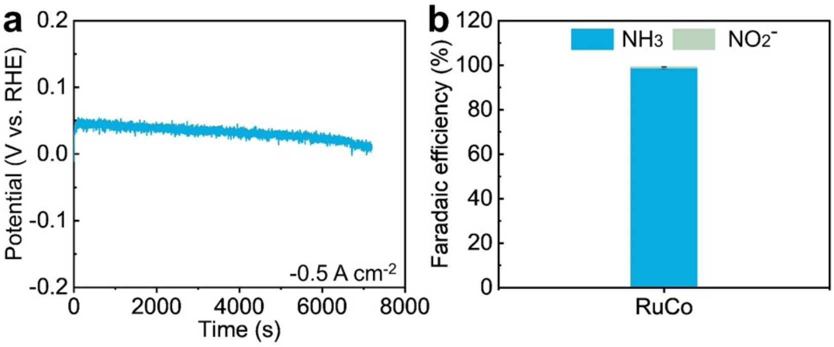

Fig. S16 (a) A chronopotentiometry curve and (b) the corresponding Faradaic efficiency plot of the RuCo catalyst under -500 mA cm^{-2} in a 1 M KOH/0.1 M KNO_3 electrolyte.

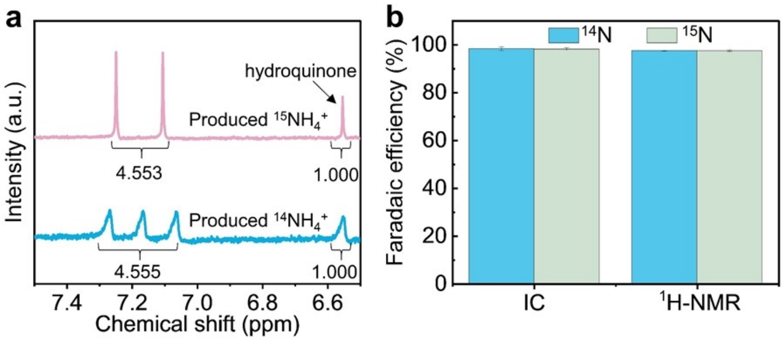

Fig. S17 (a) ^1H NMR spectra and (b) the calculated ammonia Faradaic efficiency of the RuCo catalyst *via* IC and ^1H NMR measurements under -250 mA cm^{-2} in a 1 M KOH electrolyte mixed with 0.1 M $K^{14}NO_3$ or $K^{15}NO_3$.

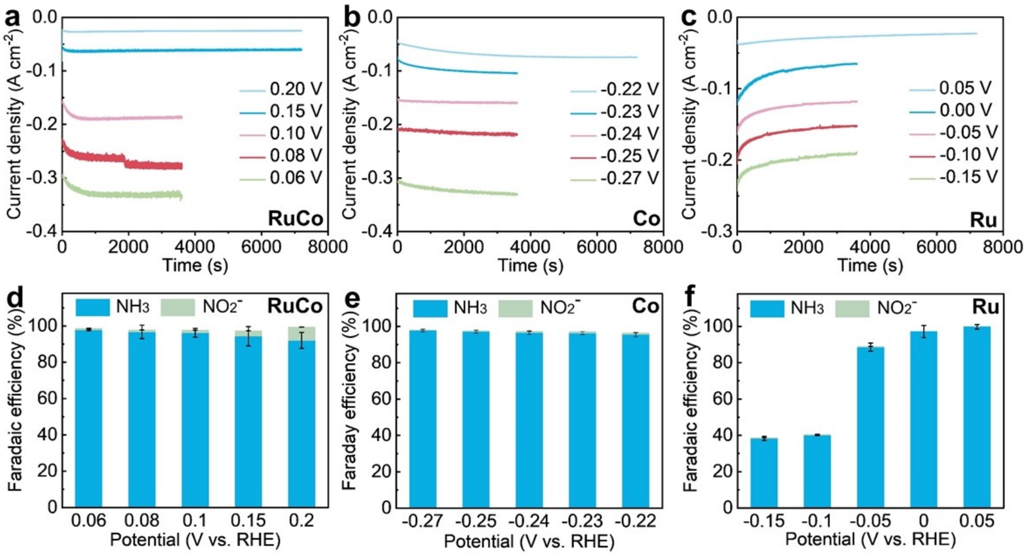

Fig. S18 Chronoamperometry curves and the corresponding Faradaic efficiency plots of (a, d) the RuCo, (b, e) Co and (c, f) Ru metals in different potential ranges.

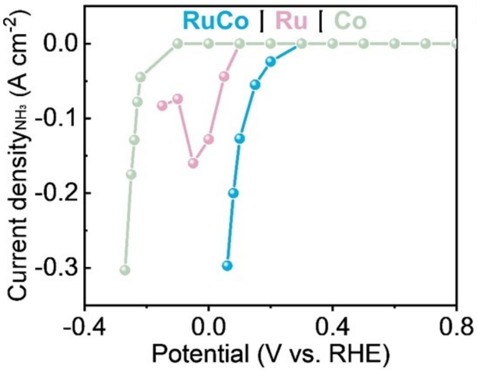

Fig. S19 NtrRR polarization curves normalized by ammonia Faradaic efficiency of the RuCo, Ru and Co metals in a 1 M KOH/KNO_3 mixed electrolyte.

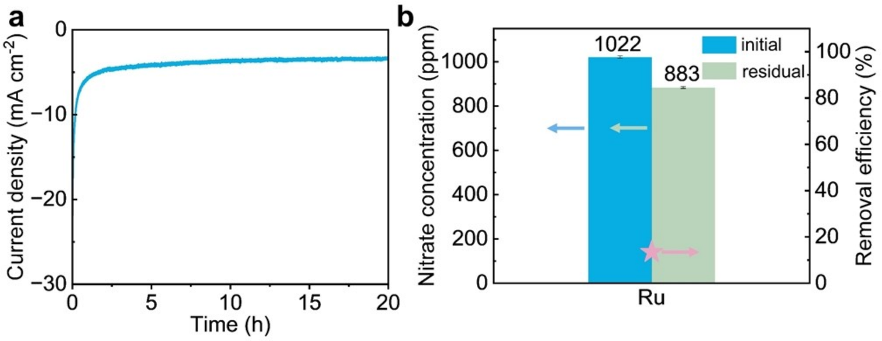

Fig. S20 (a) A chronoamperometry curve of the Ru metal at a fixed potential of 0 V *vs.* RHE (without iR_s correction) in 1 M KOH with 1000 ppm nitrate. (b) Nitrate concentration before and after the test as well as nitrate removal efficiency.

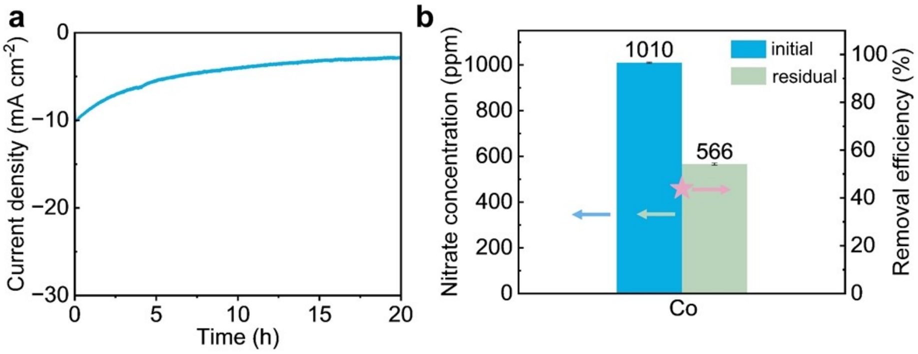

Fig. S21 (a) A chronoamperometry curve of the Co metal at a fixed potential of 0 V *vs.*

RHE (without iR_s correction) in 1 M KOH with 1000 ppm nitrate. (b) Nitrate concentration before and after the test as well as nitrate removal efficiency.

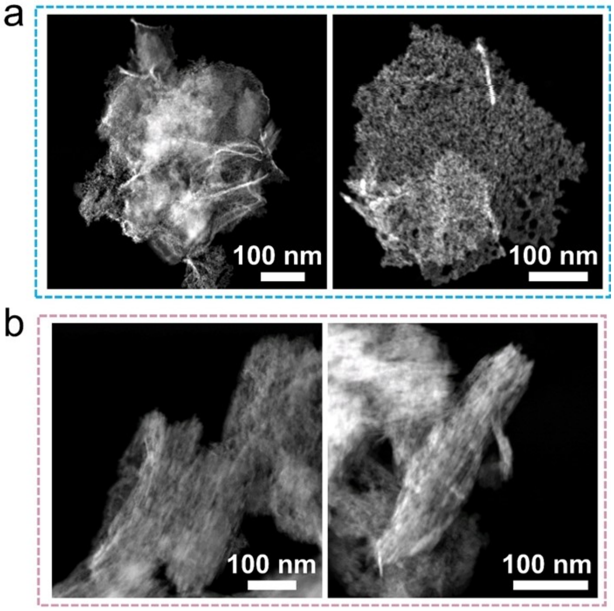

Fig. S22 HAADF-STEM images of Ru/Co$(OH)_2$ heterostructure (a) "original" nanosheets and (b) newly formed stacked nanosheets.

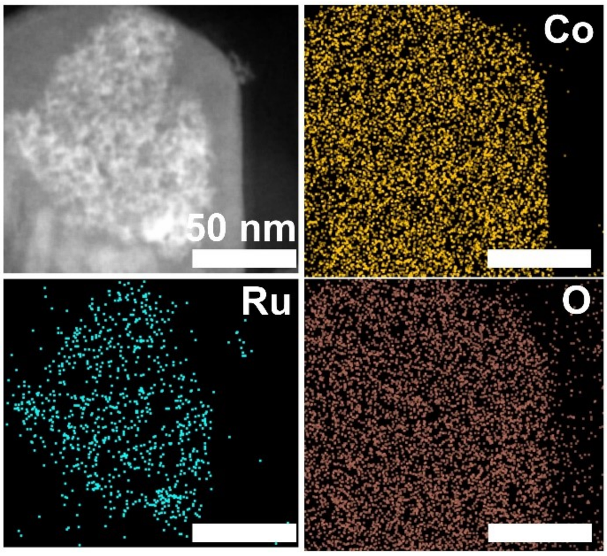

Fig. S23 A planar HAADF-STEM image and the corresponding elemental maps of stacked nanosheets observed in the RuCo catalyst after the NtrRR.

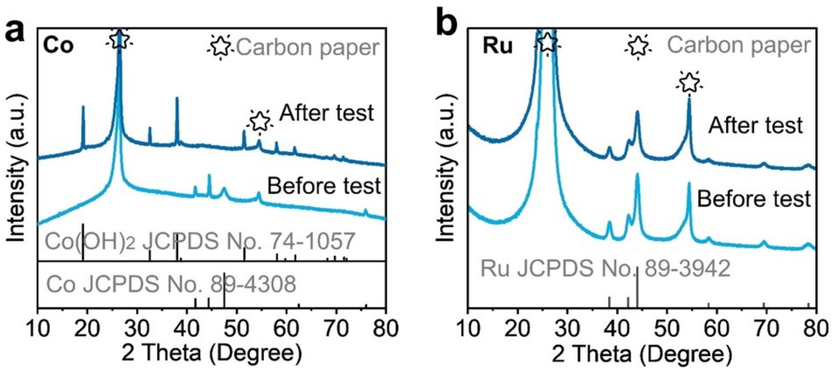

Fig. S24 XRD patterns of (a) the Co and (b) Ru metals before and after the chronopotentiometry tests.

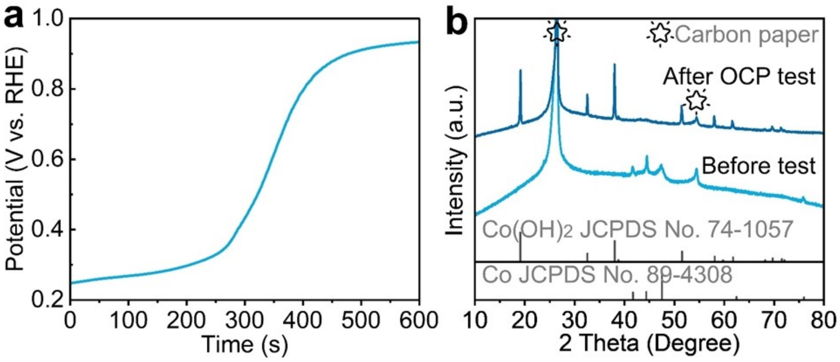

Fig. S25 (a) The open circuit potential (OCP) curve of the RuCo catalyst in 1 M KOH/0.1 M KNO_3, and (b) the XRD patterns before and after the OCP test.

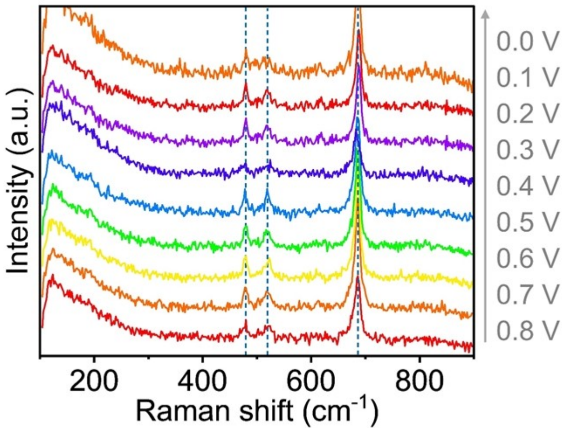

Fig. S26 *In situ* Raman curves of the RuCo catalyst from 0.8 to 0 V *vs.* RHE (without iR_s correction) in 1 M KOH/0.1 M KNO_3.

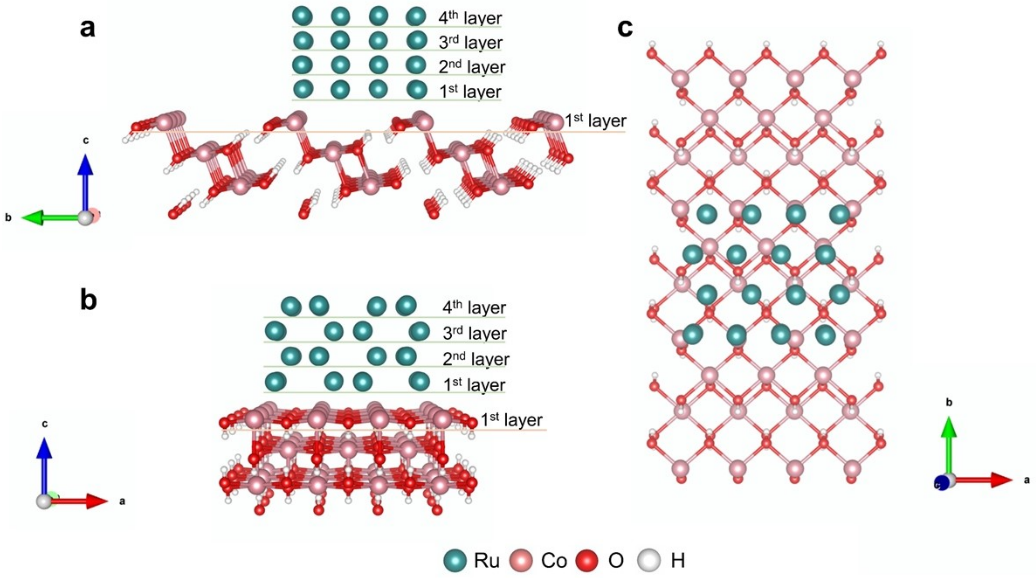

Fig. S27 Simulative structure models of Ru/β-$Co(OH)_2$ heterostructure projected from (a) *a*, (b) *b*, and (c) *c* axes.

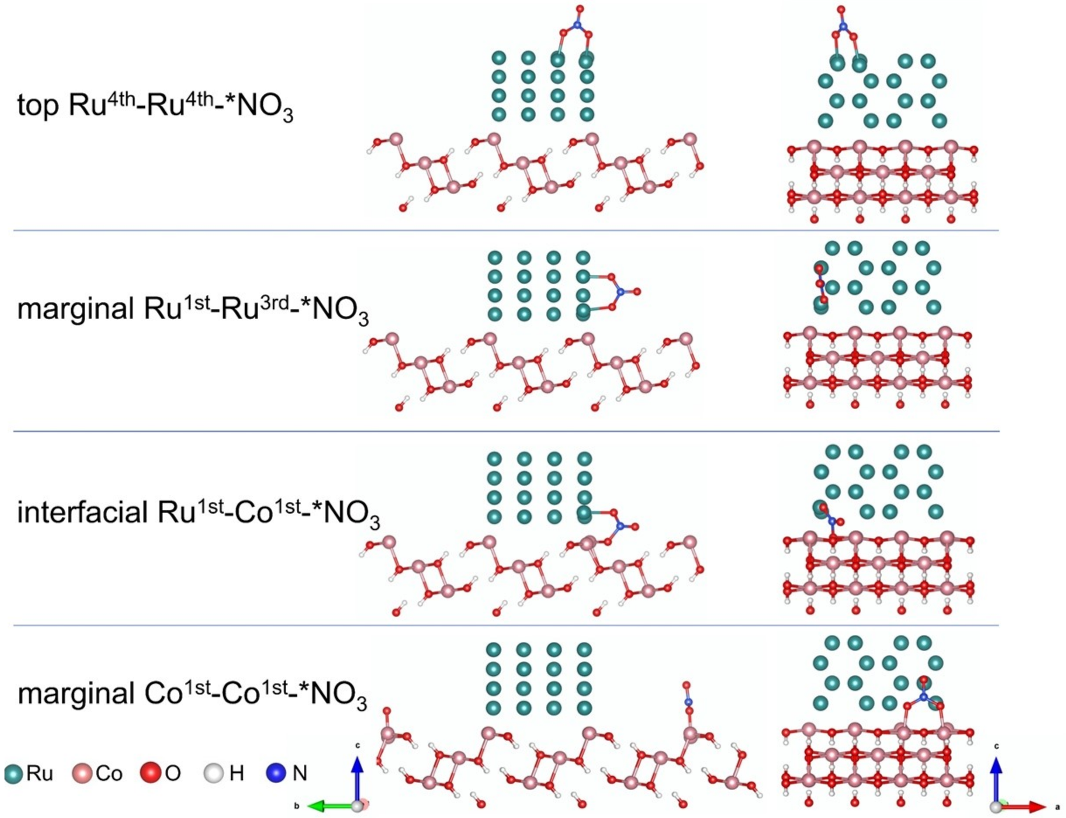

Fig. S28 $*NO_3$ dual-site adsorption models of the top Ru^{4th}-Ru^{4th}, marginal Ru^{1st}-Ru^{3rd}, interfacial Ru^{1st}-Co^{1st} and marginal Co^{1st}-Co^{1st}.

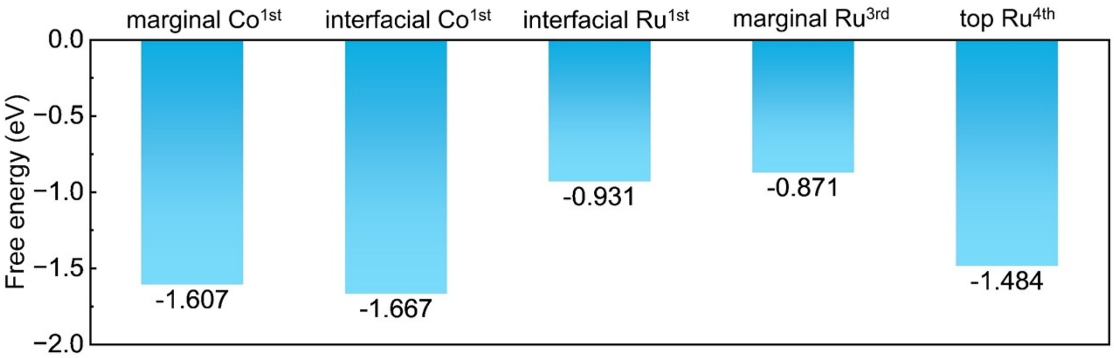

Fig. S29 Free energy diagrams of water radical dissociation (*H_2O → *H + *OH) of different sites (*i.e.*, marginal Co^{1st}, interfacial Co^{1st}, interfacial Ru^{1st}, marginal Ru^{3rd} and top Ru^{4th}) in the Ru/β-$Co(OH)_2$ in alkaline condition.

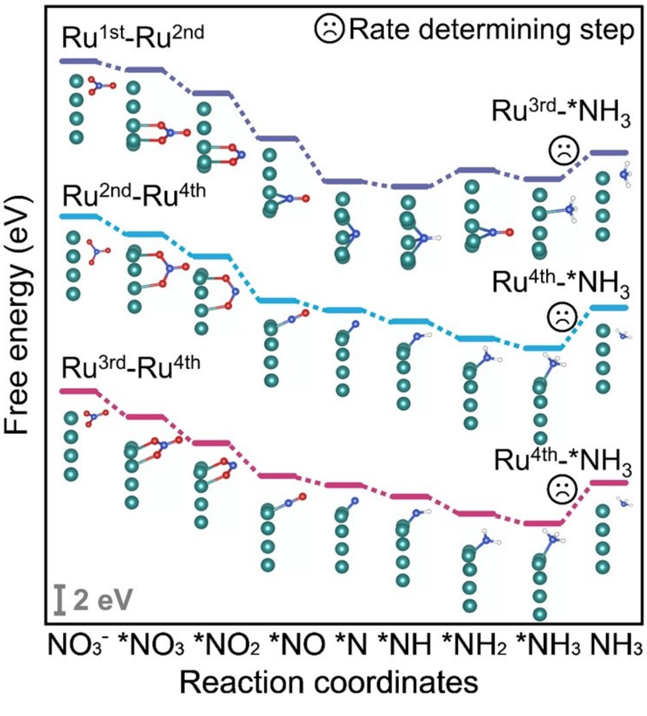

Fig. S30 NtrRR free energy diagrams and adsorption models of the marginal Ru^{1st}-Ru^{2nd}, Ru^{2nd}-Ru^{4th} and Ru^{3th}-Ru^{4th} configurations in the Ru/β-$Co(OH)_2$ heterostructure.

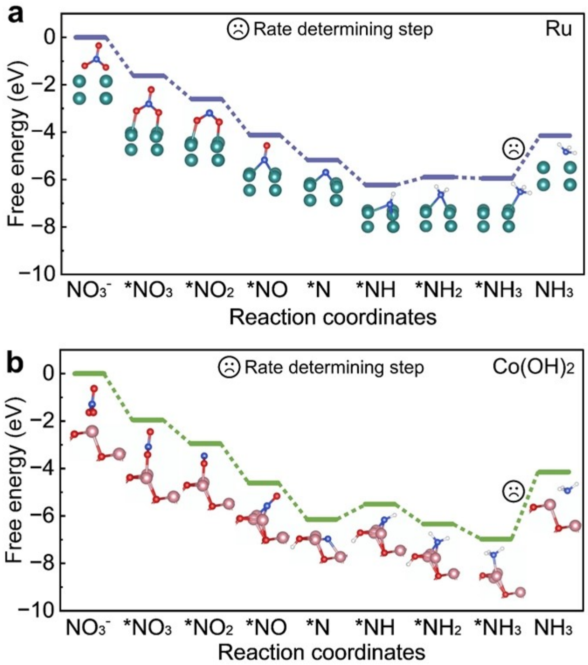

Fig. S31 Free energy diagrams and adsorption models of (a) the Ru metal and (b) β-$Co(OH)_2$.

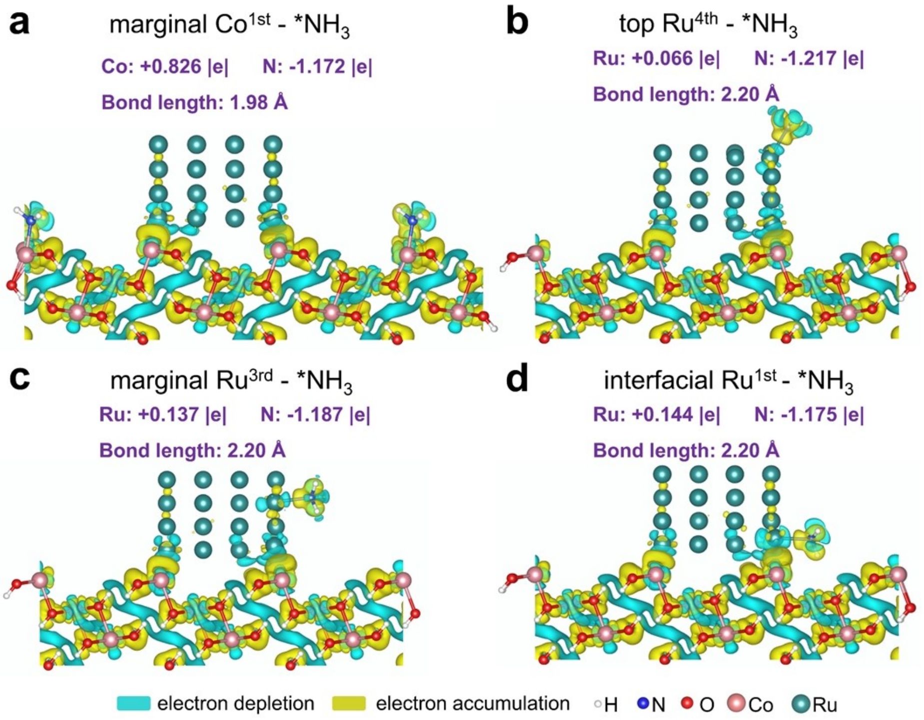

Fig. S32 Differential charge density plots, Bader charge and bond length of the four metal-$*NH_3$ desorption models of the Ru/β-$Co(OH)_2$ heterostructure (*i.e.*, (a) marginal

Co^{1st}-*NH$_3$, (b) top Ru^{4th}-*NH$_3$, (c) marginal Ru^{3rd}-*NH$_3$ and (d) interfacial Ru^{1st}-*NH$_3$).

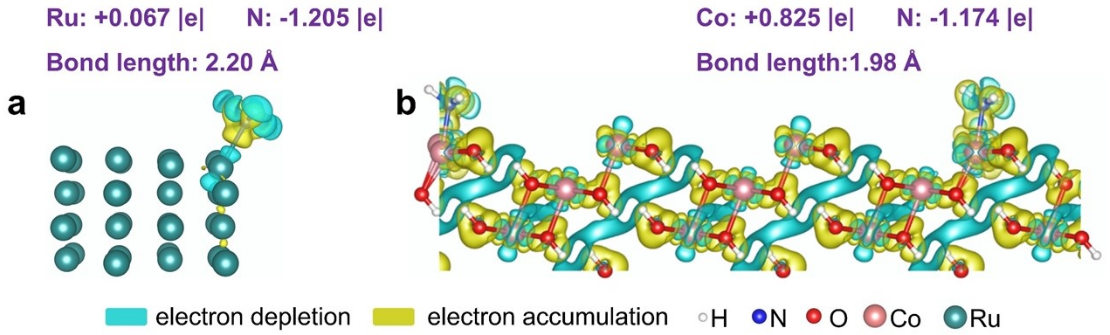

Fig. S33 Differential charge density plots, Bader charge and bond length of (a) Ru-*NH$_3$ in the Ru metal and (b) Co-*NH$_3$ in the β-Co(OH)$_2$.

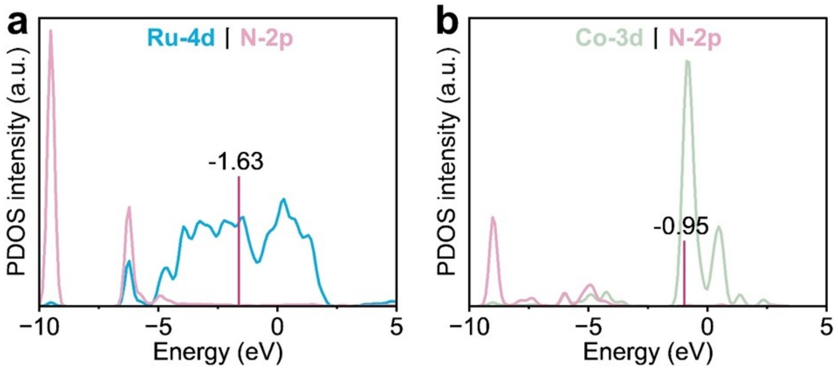

Fig. S34 PDOS diagrams of (a) the Ru-*NH$_3$ model in the Ru metal and (b) Co-*NH$_3$ model in the β-Co(OH)$_2$. Vertical lines represent the d band centers of the corresponding metal sites.

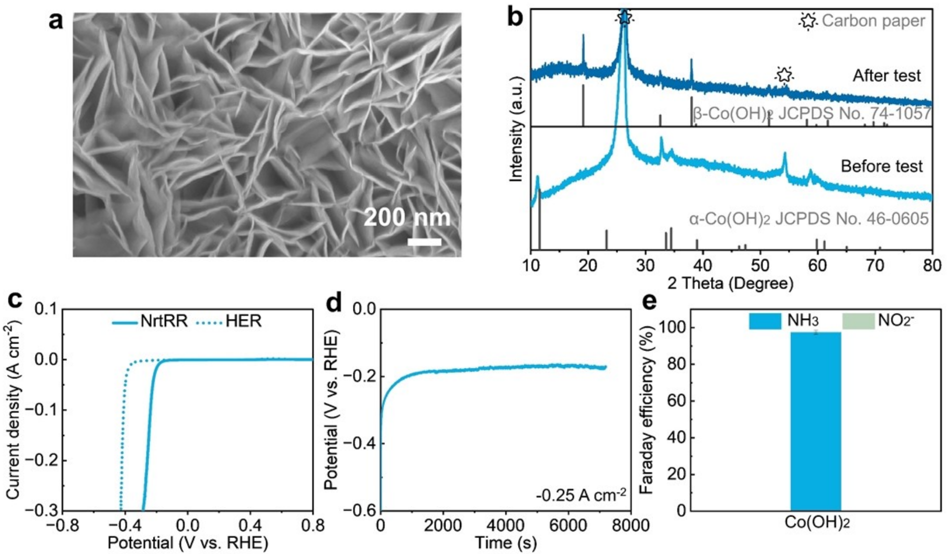

Fig. S35 Physical characterizations and electrochemical tests of electrodeposited $Co(OH)_2$. (a) A SEM image. (b) XRD patterns before and after stability tests. (c) NtrRR and HER polarization curves in 1 M KOH with or without 0.1 M KNO_3. (d) A chronopotentiometry curve under -250 mA cm^{-2} in a 1 M KOH/KNO_3 electrolyte and (e) the corresponding Faradaic efficiency.

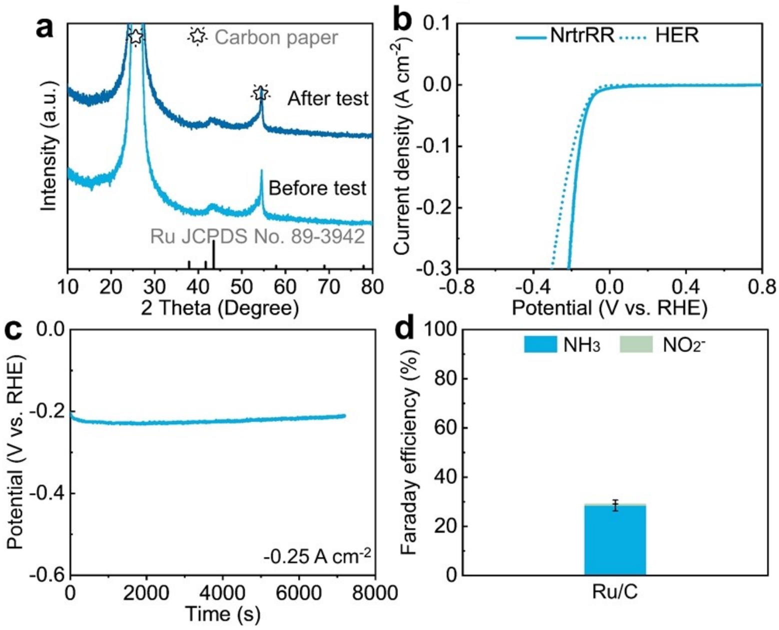

Fig. S36 Physical characterizations and electrochemical tests of the commercial 5 wt% Ru/C. (a) XRD patterns before and after chronopotentiometry tests. (b) NtrRR and HER polarization curves in 1 M KOH with or without 0.1 M KNO_3. (c) A chronopotentiometry curve under -250 mA cm^{-2} in a 1 M KOH/KNO_3 electrolyte and (d) the corresponding Faradaic efficiency.

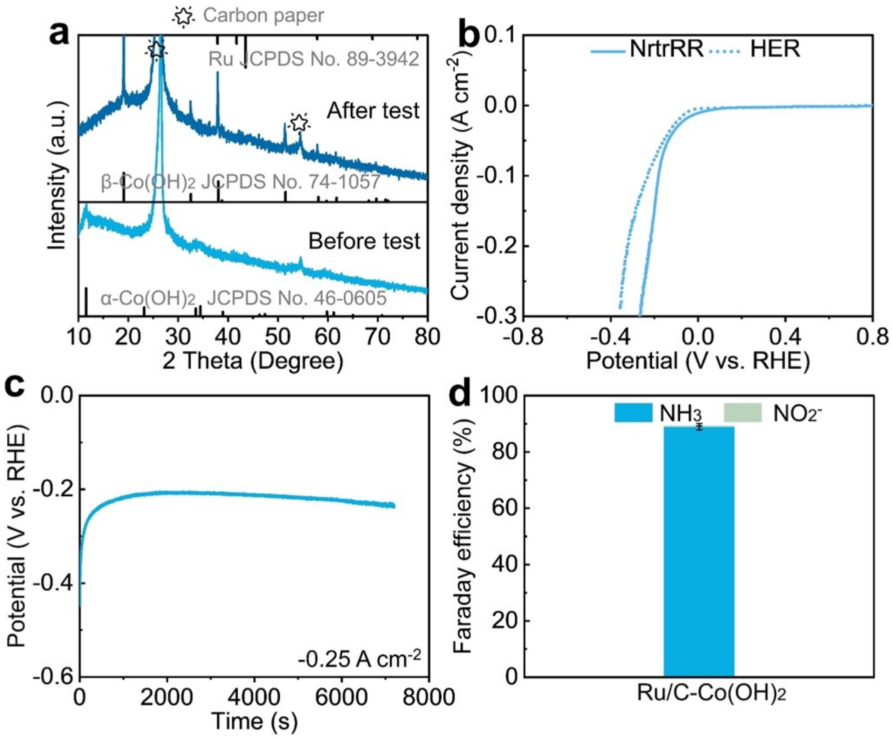

Fig. S37 Physical characterizations and electrochemical tests of the Ru/C-Co(OH)$_2$. (a) XRD patterns before and after chronopotentiometry tests. (b) NtrRR and HER polarization curves in 1 M KOH with or without 0.1 M KNO$_3$. (c) A chronopotentiometry curve under -250 mA cm^{-2} in a 1 M KOH/KNO$_3$ electrolyte and (d) the corresponding Faradaic efficiency.

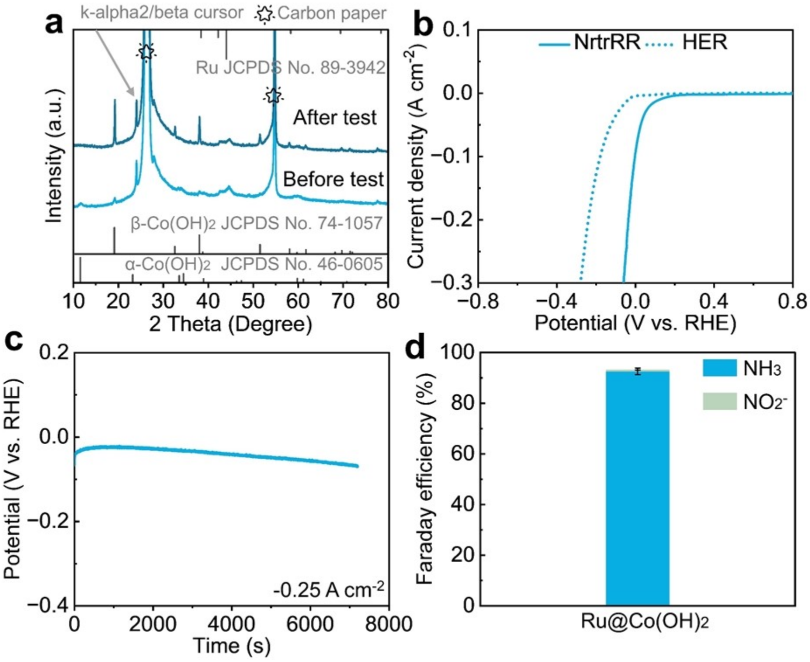

Fig. S38 Physical characterizations and electrochemical tests of the Ru@Co(OH)$_2$. (a) XRD patterns before and after chronopotentiometry tests. (b) NtrRR and HER polarization curves in 1 M KOH with or without 0.1 M KNO$_3$. (c) A chronopotentiometry curve under -250 mA cm^{-2} in a 1 M KOH/KNO$_3$ electrolyte and (d) the corresponding Faradaic efficiency.

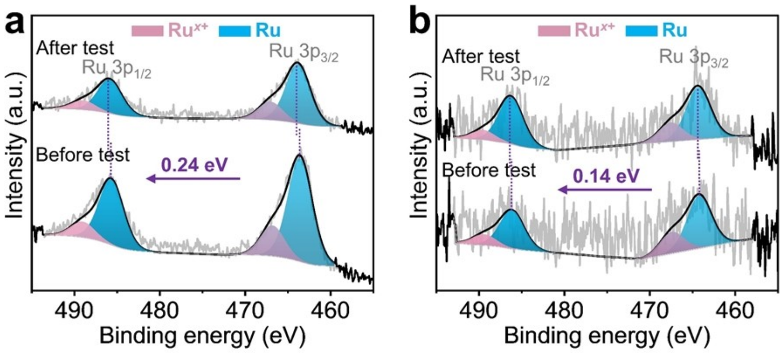

Fig. S39 Ru 3p XPS spectra of the (a) Ru@Co(OH)$_2$ and (b) Ru/C-Co(OH)$_2$ before and after the chronopotentiometry tests.

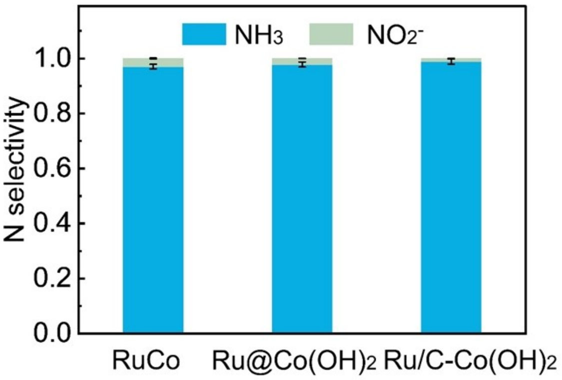

Fig. S40 N selectivity plots of the RuCo, Ru/C-Co(OH)$_2$ and Ru@Co(OH)$_2$ catalysts.

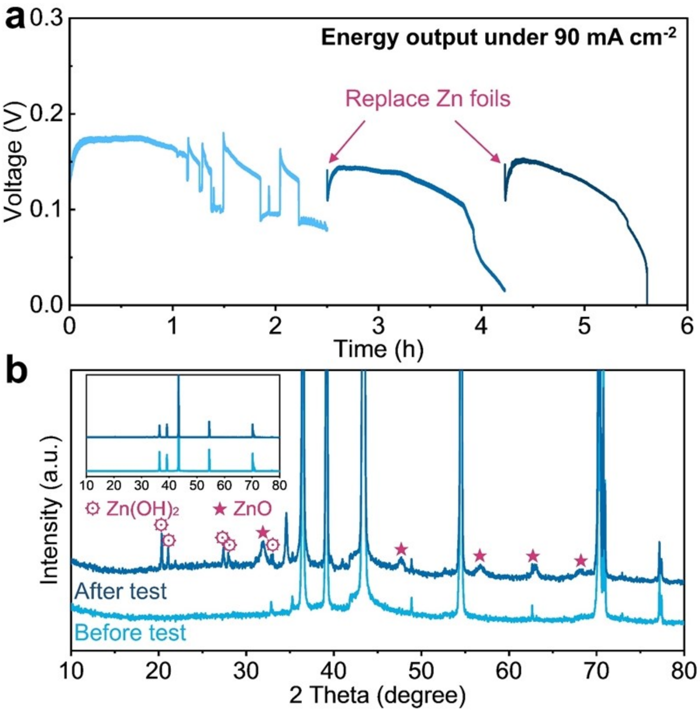

Fig. S41 (a) Chronopotentiometry curves of the Zn-nitrate flow battery using 1 M KOH as anolyte and 1 M KOH/0.1 M KNO$_3$ as catholyte under 90 mA cm^{-2} energy output. (b) Enlarged XRD patterns of Zn foil before and after the test. Inset of (b) is the XRD full pattern.

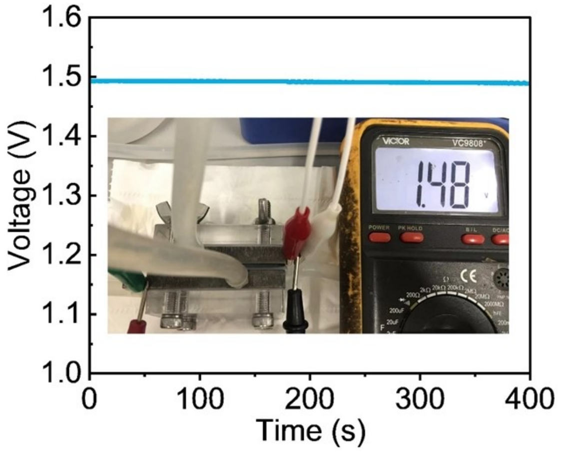

Fig. S42 An open circuit voltage curve of the Zn-nitrate flow battery, inset shows the digital image of the measured voltage by multimeter.

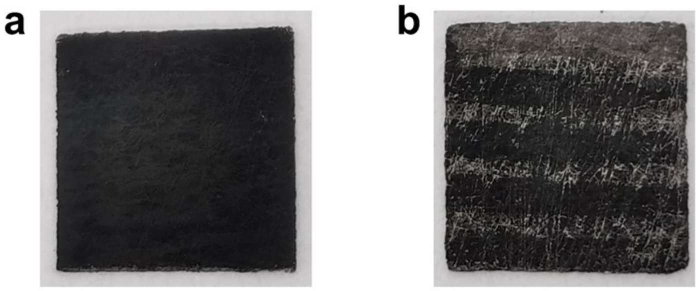

Fig. S43 Digital images of the RuCo electrode (a) before and (b) after the chronopotentiometry test in Zn-nitrate flow battery.

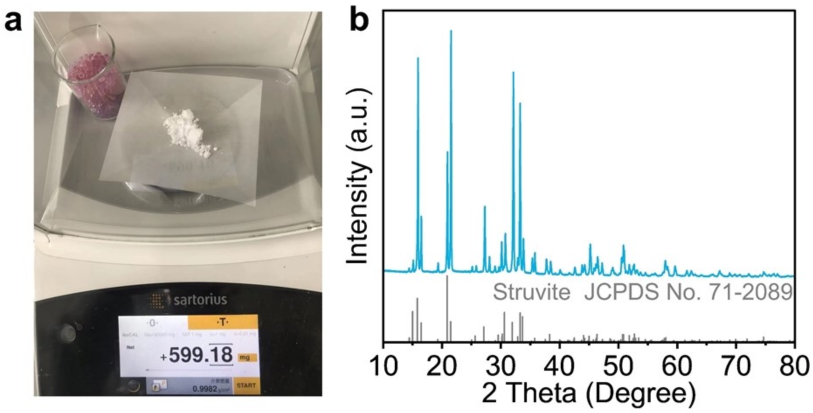

Fig. S44 (a) A digital image and (b) XRD pattern of the obtained struvite ($MgNH_4PO_4 \cdot 6H_2O$).

Additional Tables

Table S1. Comparison of the NtrRR performance of the RuCo and other recently reported high-performance catalysts.

Catalyst	**Electrolyte**	**Activity**	**Ammonia Faradaic efficiency**	**Ammonia yield rate**	**Reference**
RuCo	1 M KOH + 0.1 M KNO_3	-26 mA cm^{-2}@ 0.20 V *vs.* RHE -250 mA cm^{-2} @ 0.071 V *vs.* RHE -500 mA cm^{-2} @ 0.01 V *vs.* RHE	92.03% @ 0.20 V *vs.* RHE 98.40% @ 0.071 V *vs.* RHE 98.78% @ 0.01 V *vs.* RHE	0.13 mmol h^{-1} cm^{-2} @ 0.20 V *vs.* RHE 1.15 mmol h^{-1} cm^{-2} @ 0.07 V *vs.* RHE 2.30 mmol h^{-1} cm^{-2} @ 0.01 V *vs.* RHE	This work
Strained Ru nanoclusters	1 M KOH + 1 M KNO_3	~-100 mA cm^{-2} @ -0.2 V *vs.* RHE	~100% @ -0.2 V *vs.* RHE	1.17 mmol h^{-1} cm^{-2} @ ~130 mA cm^{-2}	*J. Am. Chem. Soc.* **2020**, *142*, 7036
CoO_x	0.1 M KOH + 0.1 M KNO_3	~-5 mA cm^{-2} @ -0.3 V *vs.* RHE	93.4% @ -0.3 V *vs.* RHE	0.33 mmol h^{-1} cm^{-2} @ -0.3 V *vs.* RHE	*ACS Catal.* **2021**, *11*, 15135
Fe-cyano-R NSs	1 M KOH + 0.1 M KNO_3	~-350 mA cm^{-2} @ -0.5 V *vs.* RHE	85−91% @ -0.5 V *vs.* RHE	1.24 mmol h^{-1} cm^{-2} @ -0.5 V *vs.* RHE	*ACS Nano* **2022**, *16*, 1072
Co-NAs	1 M KOH + 0.1 M KNO_3	-500 mA cm^{-2} @ -0.1 V *vs.* RHE	＞97% @ 0.06~-0.24 V *vs.* RHE	4.16 mmol h^{-1} cm^{-2} @ -0.14 V *vs.* RHE	*Adv. Sci.* **2021**, *8*, 2004523
RuCu	1 M KOH + 0.032 M KNO_3	-600 mA cm^{-2} @ 0 V *vs.* RHE	96% @ 0 V *vs.* RHE	~2.5 mmol h^{-1} cm^{-2} @ 0 V *vs.* RHE	*Nat. Nanotechnol.* **2022**, *17*, 759
$Ru_1/TiO_x/Ti$	1 M KOH + 0.5 M $NaNO_3$	-90 mA cm^{-2} @ -0.3 V *vs.* RHE	87.6% @ -0.3 V *vs.* RHE	/	*Angew. Chem. Int. Ed.* **2022**, *61*, 202208215
Fe/Ni_2P	0.2 M K_2SO_4 + 0.05 M KNO_3	~-50 mA cm^{-2} @ -0.4 V *vs.* RHE	94.3% @ -0.4 V *vs.* RHE	0.25 mmol h^{-1} cm^{-2} @ -0.4 V *vs.* RHE	*Adv. Energy Mater.* **2022**, 2103872
Cu nanosheets	0.1 M KOH + 0.01 M KNO_3	~-10 mA cm^{-2} @ -0.15 V *vs.* RHE	99.7% @ -0.15 V *vs.* RHE	0.02 mmol h^{-1} cm^{-2} @ -0.15 V *vs.* RHE	*Appl. Mater. Today* **2020**, *19*, 100620
CoFe LDH	1 M KOH + 1 M KNO_3	~-100 mA cm^{-2} @ -0.2 V *vs.* RHE	97.68% @ -0.45 V *vs.* RHE	0.9 mmol h^{-1} cm^{-2} @ -0.45 V *vs.* RHE	*Chem. Eng. J.* **2022**, *434*, 13464
Pd/TiO2	1M LiCl + 0.25 M KNO_3	~-20 mA cm^{-2} @ -0.7 V *vs.* RHE	92.1% @ -0.7 V *vs.* RHE	0.066 mmol h^{-1} cm^{-2} @ -0.7 V *vs.* RHE	*Energy Environ. Sci.* **2021**, *14*, 3938
Cu-NBs-100	1 M KOH + 0.1 M KNO_3	-288 mA cm^{-2} @ -0.15 V *vs.* RHE	95.3% @ -0.15 V *vs.* RHE	1.3 mmol h^{-1} cm^{-2} @ -0.15 V *vs.* RHE	*Energy Environ. Sci.* **2021**, *14*, 4989
Fe-PPy SACs	0.1 M KOH + 0.1 M KNO_3	~-30 mA cm^{-2} @ -0.6 V *vs.* RHE	100% @ -0.6 V *vs.* RHE	0.12 mmol h^{-1} cm^{-2} @ -0.6 V *vs.* RHE	*Energy Environ. Sci.* **2021**, *14*, 3522
CoP NAs	1 M KOH + 1 M KNO_3	~-200 mA cm^{-2} @ -0.3 V *vs.* RHE	~100% @ -0.3 V *vs.* RHE	0.956 mmol h^{-1} cm^{-2} @ -0.3 V *vs.* RHE	*Energy Environ. Sci.* **2022**,*15*, 760-770
$Cu_{50}Ni_{50}$	1 M KOH + 0.1 M KNO_3	-41.6 mA cm^{-2} @ -0.19 V *vs.* RHE	~99% @ -0.19 V *vs.* RHE	/	*J. Am. Chem. Soc.* **2020**, *142*, 5702
Fe_3O_4/SS	0.1 M NaOH + 0.1 M $NaNO_3$	~-120 mA cm^{-2} @ -0.5 V *vs.* RHE	91.5% @ -0.5 V *vs.* RHE	0.60 mmol h^{-1} cm^{-2} @ -0.5 V *vs.* RHE	*Nano Res.* **2021**, *15*, 3050

Catalyst	**Electrolyte**	**Activity**	**Ammonia Faradaic efficiency**	**Ammonia yield rate**	**Reference**
Fe SAC	1 M KOH + 0.1 M KNO_3	-60.7 mA cm^{-2} @ -0.21 V *vs.* RHE	86% @ -0.21 V *vs.* RHE	~0.60 mmol h^{-1} cm^{-2} @ -0.21 V *vs.* RHE	*Nat. Commun.* **2021**, *12*, 2870
PTCDA/O-Cu	0.1 M PBS + 8.06 mM KNO_3	~-15 mA cm^{-2} @ -0.4 V *vs.* RHE	~50% @ -0.4 V *vs.* RHE	~0.04 mmol h^{-1} cm^{-2} @ -0.4 V *vs.* RHE	*Nat. Energy* **2020**, *5*, 605
Co-doped Fe/Fe_2O_3	0.1 M Na_2SO_4 + 0.036 M $NaNO_3$	~-18 mA cm^{-2} @ -0.75 V *vs.* RHE	85.2 ± 0.6% @ -0.75 V *vs.* RHE	~0.05 mmol h^{-1} cm^{-2} @ -0.75 V *vs.* RHE	*PNAS* **2022**, *119*, 2115504119
a-RuO_2	0.5 M Na_2SO_4 + 0.014 M KNO_3	~-50 mA cm^{-2} @ -0.35 V *vs.* RHE	97.46% @ -0.35 V *vs.* RHE	~0.1158 mmol h^{-1} cm^{-2} @ -0.35 V *vs.* RHE	*Angew. Chem. Int. Ed.* **2022**, 202202604
Bi-Cl_{red}	1 M KOH + 0.5 M KNO_3	~-200 mA cm^{-2} @ -0.50 V *vs.* RHE	90.6% @ -0.50 V *vs.* RHE	~0.303 mmol h^{-1} cm^{-2} @ -0.50 V *vs.* RHE	*ACS Nano*, **2022**, *16*, 4795
$CuCoS_x$	0.1 M KOH + 0.1 M KNO_3	~-300 mA cm^{-2} @ -0.175 V *vs.* RHE	93.3 ± 2.1% @ -0.175 V *vs.* RHE	~1.17 mmol h^{-1} cm^{-2} @ -0.175 V *vs.* RHE	*Nat. Commun.* **2022**, *13*, 1129
$CoAl_2O_4$	0.1 M PBS + 0.1 M KNO_3	~-90 mA cm^{-2} @ -0.7 V *vs.* RHE	92.6% @ -0.7 V *vs.* RHE	~0.36 mmol h^{-1} cm^{-2} @ -0.7 V *vs.* RHE	*Chem. Eng. J.* **2022**, *435*, 135104
CoP/TiO_2	0.1 M NaOH + 0.1 M $NaNO_3$	~-70 mA cm^{-2} @ -0.3 V *vs.* RHE	95% @ -0.3 V *vs.* RHE	0.50 mmol h^{-1} cm^{-2} @ -0.3 V *vs.* RHE	*Mater. Today Phys.* **2022**, *48*, 100854
$ZnCo_2O_4$	0.1 M NaOH + 0.1 M $NaNO_3$	~-100 mA cm^{-2} @ -0.6 V *vs.* RHE	~98% @ -0.6 V *vs.* RHE	~0.46 mmol h^{-1} cm^{-2} @ -0.6 V *vs.* RHE	*Mater. Today Phys.* **2022**, *23*, 100619

Table S2. NtrRR free energy of the Ru/β-$Co(OH)_2$ heterostructure. The PDSs are marked with blue color.

Adsorption sites	NO_3^- →	$*NO_3$ →	$*NO_2$ →	$*NO$ →	$*N$ →	$*NH$ →	$*NH_2$ →	$*NH_3$ → NH_3	Desorption site
Ru^{4th}-Ru^{4th}	-1.511	-1.006	-1.567	-1.074	-0.951	0.216	-0.096	1.841	Ru^{4th}
Ru^{1st}-Ru^{3rd}	-0.420	-1.18	-1.906	-1.949	-0.225	0.743	-0.409	1.198	Ru^{3rd}
Ru^{1st}-Co^{1st}	-0.997	-1.173	-1.9	-1.791	-0.145	0.381	0.508	0.969	Ru^{1st}
Co^{1st} -Co^{1st}	-1.991	-0.981	-1.653	-1.527	0.644	-0.836	-0.648	2.844	Co^{1st}
Ru^{1st}-Ru^{2nd}	-0.385	-1.074	-2.183	-1.813	-0.225	0.743	-0.409	1.198	Ru^{3rd}
Ru^{2nd}-Ru^{4th}	-0.815	-0.999	-2.013	-0.429	-0.51	-0.783	-0.44	1.841	Ru^{4th}
Ru^{3rd}-Ru^{4th}	-1.157	-1.19	-1.48	-0.429	-0.51	-0.783	-0.44	1.841	Ru^{4th}

Table S3. NtrRR free energy of the Ru metal. The PDS is marked with blue color.

Adsorption sites	NO_3^- →	$*NO_3$ →	$*NO_2$ →	$*NO$ →	$*N$ →	$*NH$ →	$*NH_2$ →	$*NH_3$ → NH_3	Desorption site
Ru^{4th}-Ru^{4th}	-1.618	-0.989	-1.512	-1.06	-1.053	0.342	-0.062	1.804	Ru^{4th}

Table S4. NtrRR free energy of the β-$Co(OH)_2$. The PDS is marked with blue color.

Adsorption sites	NO_3^- →	$*NO_3$ →	$*NO_2$ →	$*NO$ →	$*N$ →	$*NH$ →	$*NH_2$ →	$*NH_3$ → NH_3	Desorption site
Co^{1st} -Co^{1st}	-1.951	-0.999	-1.663	-1.535	0.647	-0.839	-0.639	2.831	Co^{1st}